nature chemistry

Article

https://doi.org/10.1038/s41557-024-01620-y

Few-femtosecond electron transfer dynamics in photoionized donor–π–acceptor molecules

Received: 29 September 2023

Accepted: 30 July 2024

Published online: 25 September 2024

Check for updates

Federico Vismarra[1,2,10], Francisco Fernández-Villoria[3,4,10], Daniele Mocci[1], Jesús González-Vázquez[4], Yingxuan Wu[1,2], Lorenzo Colaizzi[1], Fabian Holzmeier[5], Jorge Delgado[3,4], José Santos[3,6], Luis Bañares[3,7], Laura Carlini[8], Mattea Carmen Castrovilli[8], Paola Bolognesi[8], Robert Richter[9], Lorenzo Avaldi[8], Alicia Palacios[4], Matteo Lucchini[1,2], Maurizio Reduzzi[1], Rocío Borrego-Varillas[2] ✉, Nazario Martín[3,6], Fernando Martín[3,4] ✉ & Mauro Nisoli[1,2] ✉

The exposure of molecules to attosecond extreme-ultraviolet (XUV) pulses offers a unique opportunity to study the early stages of coupled electron–nuclear dynamics in which the role played by the different degrees of freedom is beyond standard chemical intuition. We investigate, both experimentally and theoretically, the first steps of charge-transfer processes initiated by prompt ionization in prototype donor–π–acceptor molecules, namely nitroanilines. Time-resolved measurement of this process is performed by combining attosecond XUV-pump/few-femtosecond infrared-probe spectroscopy with advanced many-body quantum chemistry calculations. We show that a concerted nuclear and electronic motion drives electron transfer from the donor group on a sub-10-fs timescale. This is followed by a sub-30-fs relaxation process due to the probing of the continuously spreading nuclear wave packet in the excited electronic states of the molecular cation. These findings shed light on the role played by electron–nuclear coupling in donor–π–acceptor systems in response to photoionization.

The ultrafast redistribution of energy and electronic charge in molecules after photoexcitation is a phenomenon of primary relevance in physics, chemistry and materials science[1–3]. Photoinduced electron transfer (ET) and charge transfer (CT) have a great importance in nature since they govern photosynthesis in plants and bacteria[4]. Furthermore, these processes are the driving mechanisms at the heart of many fundamental processes located on the boundary between purely quantum effects and molecular dynamics: from non-adiabatic electron–nuclei correlations[5,6] and electronic decoherence[7–9] to photovoltaic response[10] and electronic transport[11]. The ability to measure the ET/CT dynamics with extreme temporal resolution not only provides a fundamental understanding of the physical mechanisms behind these processes, but also offers unique insights into how to engineer the chemical and structural properties of the molecule to control or enhance them. In this context, ultrashort extreme-ultraviolet (XUV) pulses from table-top high-order harmonic sources or free electron laser (FEL) facilities stand

[1]Department of Physics, Politecnico di Milano, Milan, Italy. [2]Institute for Photonics and Nanotechnologies, IFN-CNR, Milan, Italy. [3]Instituto Madrileño de Estudios Avanzados en Nanociencia, Madrid, Spain. [4]Departamento de Química, Universidad Autónoma de Madrid, Madrid, Spain. [5]imec, Leuven, Belgium. [6]Departamento de Química Orgánica I, Universidad Complutense de Madrid, Madrid, Spain. [7]Departamento de Química Física, Universidad Complutense de Madrid, Madrid, Spain. [8]Istituto di Struttura della Materia-CNR (ISM-CNR), Rome, Italy. [9]Sincrotrone Trieste, Area Science Park, Basovizza, Trieste, Italy. [10]These authors contributed equally: Federico Vismarra, Francisco Fernández-Villoria. ✉e-mail: rocio.borregovarillas@cnr.it; fernando.martin@uam.es; mauro.nisoli@polimi.it

as potent tools for initiating and observing, on timescales ranging from the femtosecond[12–16] down to the attosecond[2,17], a wide range of electronic/nuclear processes unfolding as an ultrafast response to photoionization. In addition, advancements in X-ray FEL technology have enabled the generation of X-ray pulses lasting a few femtoseconds[18] and even attoseconds[19], with sufficient energy for conducting X-ray-pump/X-ray-probe experiments. These capabilities provide site- and state-specific resolution, which is of particular interest for investigating CT phenomena in molecules[20].

A variety of experimental techniques have been reported in which attosecond sources have been used either as pump or as probe. Attosecond transient absorption spectroscopy (ATAS)[21], in which few-femtosecond visible (VIS) or near-infrared (NIR) pulses excite the sample and attosecond pulses probe the induced dynamics with element sensitivity, has been used to follow the dynamics mediated by conical intersections in diatomic molecules such as iodine monobromide (IBr)[22], in polyatomic molecules such as methyl bromide (CH_3Br)[23], in ethylene cation ($C_2H_4^+$)[24], methane cation (CH_4^+)[25] and in neutral silane (SiH_4)[26]. At the same time, recent advancements in generating sub-3-fs deep ultraviolet (UV) pulses[27,28] are opening interesting avenues for investigating with ATAS the initial stages of UV-induced dynamics, an area previously constrained by lower temporal resolution[29–31].

Another powerful experimental approach for accessing coupled electron–nuclear dynamics in molecules is attosecond photoelectron/ion spectroscopy, in which attosecond pulses initiate the dynamics by promptly removing an electron, and femtosecond VIS-NIR pulses probe/control the ensuing dynamics, often in a non-perturbative way. In this case, the photoelectron or the ion spectra produced by the interaction with the pump and probe pulses are measured as a function of the pump–probe time delay. This method has been employed, for example, to measure charge migration in aromatic amino acids (phenylalanine and tryptophan)[32,33], the photodissociation dynamics of the ethylene cation $C_2H_4^+$ excited by XUV pulses[34,35] and ultrafast energy relaxation following ionization induced by 20 fs XUV pulses in planar polycyclic aromatic hydrocarbons with increasing sizes[36].

Despite many ground-breaking advancements, a detailed understanding of the initial steps of ET/CT and of the ultrafast processes driven by coupled electron–nuclear motion in medium-sized and large molecules immediately after prompt photoionization is not yet available. As a consequence, precise temporal information on the various steps of the ET/CT process, often illustrated with a sequence of Lewis diagrams[37], has never been thoroughly addressed. This is mainly caused by the lack of adequate and computationally accessible methods to describe many-body quantum systems and by the limited set of experiments offering a proper time resolution on polyatomic molecules. Here we present experimental evidence, together with detailed numerical simulations, of a sub-10-fs ET process in three species of nitroaniline cations, driven by an ultrafast molecular planarization process. ET is then followed by a slower spreading of the nuclear wave packet in the excited electronic states of the molecular cation. By monitoring the production of ionic fragments and computing the temporal evolution of the electronic density in different regions of the molecular structure, we are able to time resolve the coupling between electronic and nuclear motion, hence unravelling the intrinsically joint nature of the ET process occurring at the few-femtosecond timescale.

Results and discussion

Investigated molecules

We have investigated *para*-nitroaniline (*p*-NA), *meta*-nitroaniline (*m*-NA) and *N*,*N*-dimethyl-4-nitroaniline (nd-NA), the chemical structures of which are displayed in Fig. 1a. These molecules are constituted by an electron-donating amino functional group ($-NH_2$ or $-NMe_2$) and an electron-withdrawing nitro functional group ($-NO_2$) connected through a π-conjugated benzene ring. This structural arrangement gives rise to a strong molecular dipole in which the electron density is

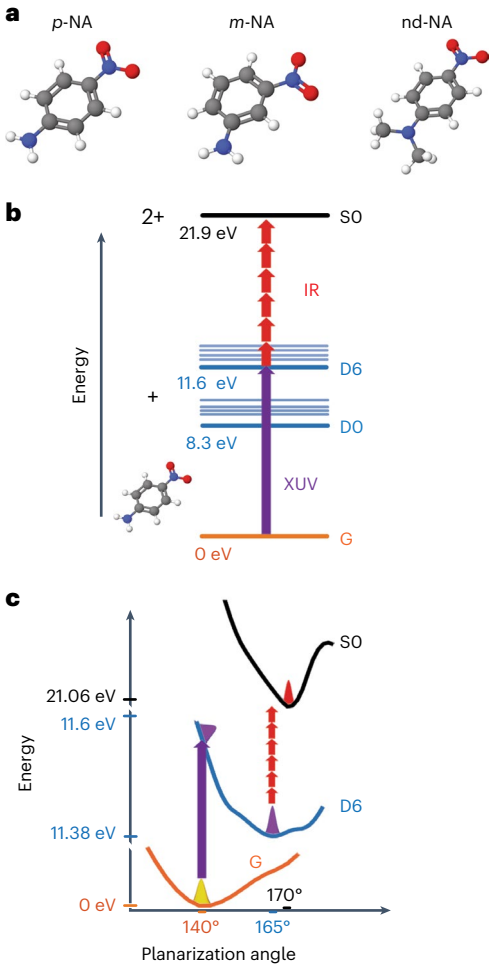

Fig. 1 | Molecular structures and experimental strategy. a, Molecular structures of *p*-NA, *m*-NA and nd-NA. Red, oxygen; blue, nitrogen; black, carbon; white, hydrogen. **b**, Scheme of the pump–probe experiment. The XUV attosecond pulse ionizes the molecule from the ground state G, thus creating a superposition of cationic states (D0, D1, ...). A delayed VIS-NIR field favours a second ionization by multiphoton absorption, creating a dication. **c**, Calculated potential energy curves versus the planarization angle of the amino group with respect to the benzene ring of the ground state, G, of the neutral *p*-NA molecule, the excited state D6 of the cation and the ground state S0 of the dication. After an initial localization into a minimum of potential in D6, the wave packet spreads over several degrees of freedom.

shifted towards the most electronegative nitro group, leaving a positive partial charge located closer to the amino group. Therefore, these molecules can be formally considered as a class of donor–π–acceptor prototypes[38–40]. The comparison between *p*-NA and *m*-NA allows us to investigate the positive (negative) inductive effect of the donor (acceptor) group on the ultrafast dynamics because the molecular dipole decreases from 15 D for *p*-NA to 6 D for *m*-NA (complete basis set method CBS-QB3)[41]. The presence of the methyl groups (CH_3) in nd-NA affects the polarity and the charge separation between the positive and negative sides of the molecule[7] and increases the electron reservoir available from the donor group due to the positive inductive effect of the methyl groups.

Molecules were ionized by isolated sub-200-as pulses generated in krypton, with photon energy in the spectral range between 20 and 50 eV (Supplementary Fig. 1b). The dynamics of the cations were then probed by 4 fs VIS-NIR pulses (central photon energy, 1.77 eV) with a peak intensity of 5×10^{12} W cm^{-2}, which can promote the cations to molecular dications via multiphoton absorption. The parent and fragment ions produced by the interaction of the molecules with the pump

https://doi.org/10.1038/s41557-024-01620-y

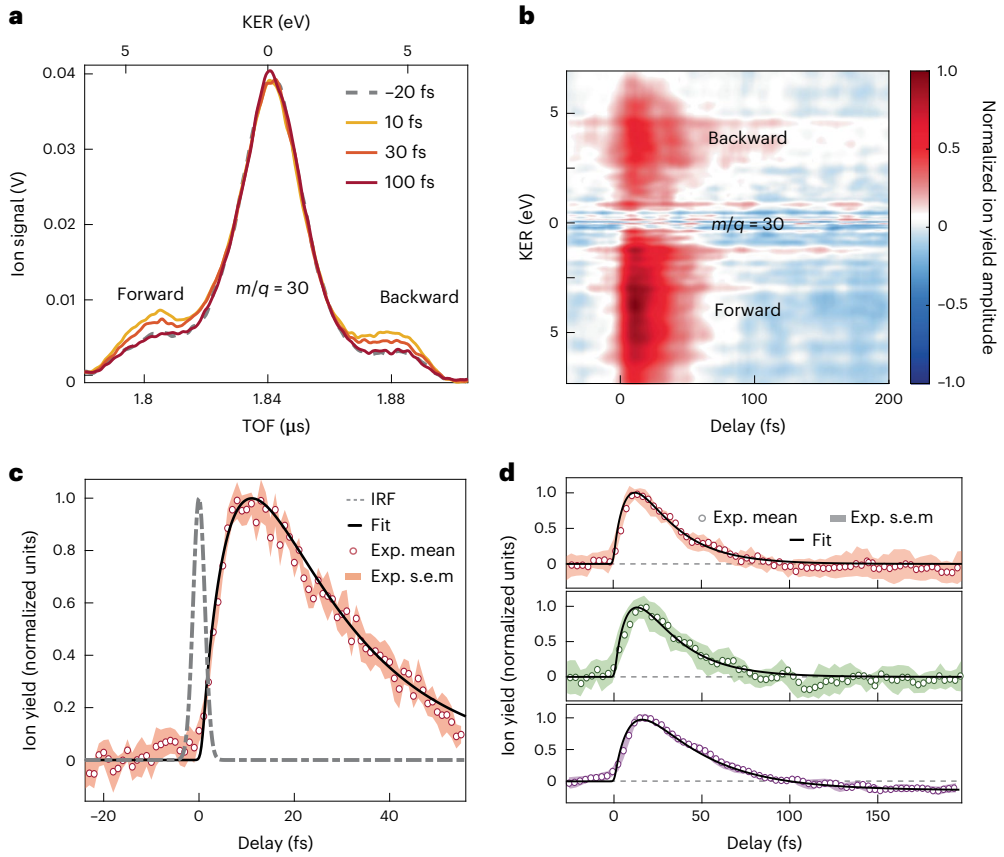

Fig. 2 | Time-resolved measurements. a, Experimental TOF spectra of NO^+ ($m/q = 30$) for different time delays between pump and probe pulses in the case of *p*-NA. The upper *x* axis displays the kinetic energy release (KER) for both forward and backward emitted ions. **b**, Normalized differential mass spectra of NO^+ for *p*-NA versus pump–probe time delay obtained by determining the difference between the spectra acquired with and without the probe pulse. **c**, NO^+ yield in the case of *p*-NA obtained by integrating the TOF spectra of the high-energy NO^+ ion emitted in the forward direction in a 3 eV kinetic energy window centred on the maximum of the corresponding shoulder. Data are presented as mean values over six acquisitions ± s.e.m, here represented as a shaded area. The black line is a fitting curve with an exponential rise time of 9.3 fs and an exponential relaxation time of 22.4 fs; the dash-dotted grey line is the impulsive response function (IRF). **d**, NO^+ yield in the case of *p*-NA (orange, same as **c**), *m*-NA (green) and nd-NA (purple) obtained by integrating the TOF spectra of the high-energy NO^+ ion emitted in the forward direction. Data are presented as mean values ± s.e.m.

and probe pulses were then collected by a linear time-of-flight (TOF) mass spectrometer.

Time-resolved measurements

The concept of the experiment is shown in Fig. 1b,c. Isolated attosecond pulses photoionize gas-phase molecules and populate several electronic states of the cation (and also a few ones of the dication), in which coupled electron and nuclear dynamics are initiated. The interaction of the VIS-NIR pulse with the cations is sensitive to these dynamics, determining the fate of the subsequent fragmentation process, which evolves on a longer timescale. Therefore, the yield of production of the different fragments as a function of the time delay between the attosecond pump pulse and the VIS-NIR probe pulse is related to the evolving dynamics in the cationic states.

In particular, the mass spectrum at mass-to-charge ratios $m/q = 30$ and 46, corresponding to the nitrosonium (NO^+) and nitronium (NO_2^+) cations, respectively, displays a characteristic structure with a central peak and two shoulders (see Fig. 2a for the case of NO^+). The two shoulders are produced by the kinetic NO^+/NO_2^+ ions emitted in the Coulomb explosion (CE) of the dication in the forward or in the backward direction relative to the detector: these ions are detected either at earlier or later times, respectively, in the TOF spectrum. The corresponding kinetic energy release is reported on the upper *x* axis of Fig. 2a and on the *y* axis of Fig. 2b. This assignment was further corroborated by synchrotron measurements (Methods). Figure 2a,b illustrates that only the shoulders exhibit a temporal evolution, in contrast to the central peak, which remains unchanged with varying pump–probe delay. This observation confirms that the two shoulders and the central peak arise from distinct mechanisms. The dynamics on the side peaks are directly associated with a time-dependent variation of the molecular dication population. On the contrary, the central peak can be ascribed to an independent dissociation process occurring at the cationic level, barely affected by the VIS-NIR probe pulses. The evolution of the NO^+ yield, obtained by integrating the TOF spectra of the ions emitted in the forward direction in a 3 eV kinetic energy window centred on the maximum of the corresponding shoulder, is shown in Fig. 2c on a 50 fs timescale and on a longer timescale (200 fs) in Fig. 2d. The experimental data display a rise time $\tau_1 = 9.3 \pm 1.4$ fs and an exponential decay with time constant $\tau_2 = 22.4 \pm 1.2$ fs and the corresponding fitting curves are shown as black lines in Fig. 2c,d. The same behaviour was obtained in the case of the NO_2^+ fragment ($m/q = 46$) in the kinetic energy window centred on the maximum of the shoulder corresponding to the high-energy ions (as shown in Supplementary Fig. 5). The ultrafast dynamics of the NO^+ and NO_2^+ fragments of *m*-NA and nd-NA show the same features, as displayed in Fig. 2d (the measured rise time and relaxation lifetime for the three molecules are reported in Supplementary Table 1). A temporal evolution was also observed in other charged fragments. It is worth mentioning that the yield of production of the fragments CN^+ ($m/q = 26$), C_2N^+ ($m/q = 38$) and C_3N^+ ($m/q = 50$) has a rise time comparable to that measured for NO^+ and

https://doi.org/10.1038/s41557-024-01620-y

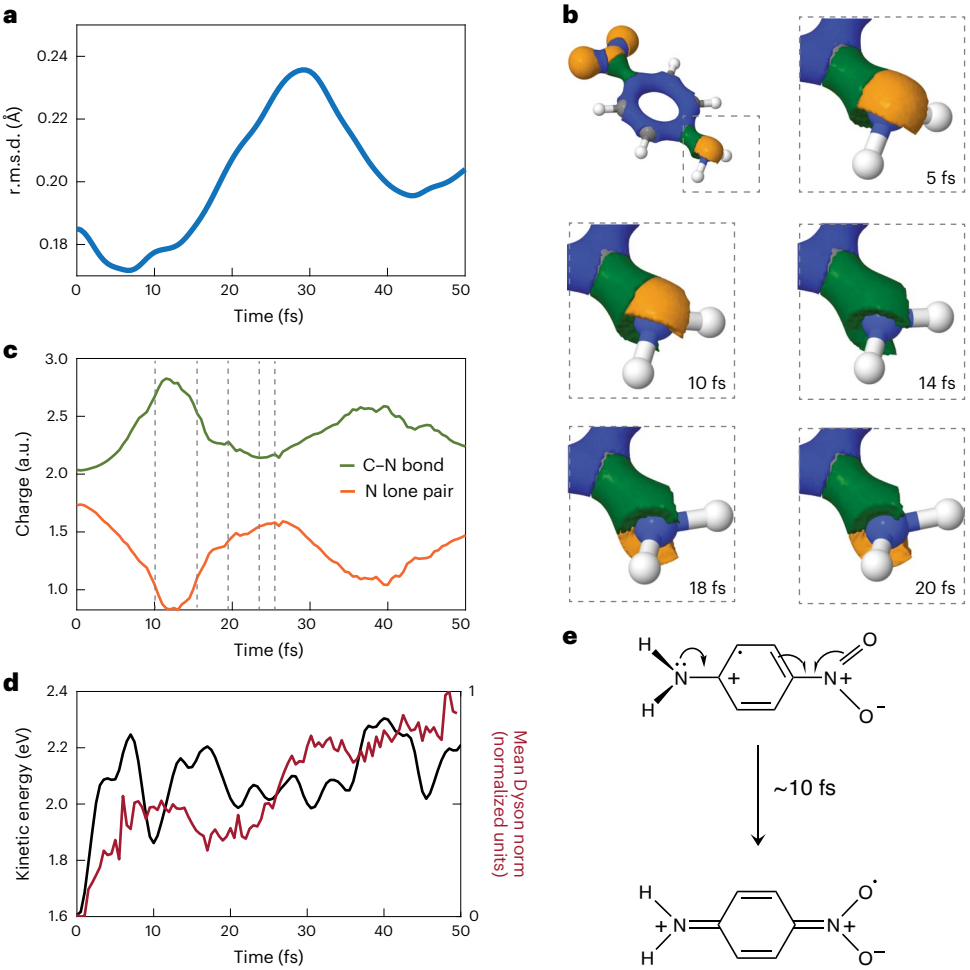

Fig. 3 | Sub-10-fs planarization process. a, Calculated temporal evolution of the average r.m.s.d. of all the trajectories initialized in electronic state D6 of *p*-NA with respect to the planar minimum geometry. The lower the values of the r.m.s.d, the closer to the planar geometry. **b**, Snapshots of the evolution of the electronic density. The colours indicate the basins where the density is assigned. In the NH_2 region, orange indicates the lone pair of the nitrogen; green indicates the C–N bond. **c**, Temporal evolution of the average charge in the ELF basins for the lone pair of the nitrogen N in the NH_2 group (orange) and the C–N bond connecting it to the ring (green). **d**, Temporal evolution of the average kinetic energy of the nuclear wave packet (black curve) and the average Dyson norm (red curve) corresponding to the orbital that results from the projection of the whole wave packet in the monocation at each time-step of the surface hopping trajectory onto the dication. **e**, Lewis structures representing the CT from the lone pair of the nitrogen to the adjacent C–N bond and from the NO_2 group to the other C–N bond.

NO_2^+ fragments ($\tau_1 \approx 10$ fs) and a subsequent much longer relaxation lifetime (Supplementary Table 1).

Theoretical calculations

Due to the large bandwidth of the attosecond pulse used to ionize the molecules (~20 eV), many electronic states in the resulting molecular cation are energetically accessible. However, according to our measured photoelectron spectra (PES), recorded with synchrotron radiation at 60 eV (Extended Data Fig. 1), the major contributions to the PES come from the lowest electronic states for all three molecular cations. Our theoretical multireference complete active space self-consistent field calculations[42] confirm that the largest Dyson norms at the equilibrium geometry of the neutral molecule mainly correspond to states of the monocation lying up to 4 eV above the ionization threshold, all of them with a pronounced 1 hole (1h) character. This is further supported by the reasonable agreement between measured and calculated spectra, the latter obtained from actual ionization probabilities or the Dyson norms (Supplementary Figs. 11 and 13).

Consequently, to understand the origin of the measured ultrafast dynamics in each molecular cation, we have mostly considered these low-lying cationic states as starting points for the ensuing coupled electron–nuclear dynamics. These dynamics were described by performing few-switches trajectory surface hopping calculations as implemented in the SHARC code[43], in which nuclear motion is described classically in the potential energy surfaces of the lowest ten electronic states (which include all 1h states and most of the 2 hole–1 particle (2h–1p) and a few 2h–2p states in the 0-4 eV energy interval) and all possible non-adiabatic transitions among them are taken into account. In all cases, the initial geometry in these dynamics simulations was that of the neutral molecule.

Let us first consider the case of the *p*-NA cation. As the charge dynamics initiated from different states of this cation (those with the largest Dyson norms) is qualitatively similar, here we will only show the results for trajectories starting in the D6 state. Results obtained by starting from the D1, D2 and D50 states, which are the main contributors to the spectral region covered by the broadband attosecond pulse (Supplementary Table 3), are shown in Supplementary Fig. 15. The first important result of the simulation is that, immediately after photoionization, the cation undergoes an ultrafast planarization of the amino group (NH_2) with the benzene ring, irrespective of the initial electronic state of the cation, including its ground state. Figure 3a shows the temporal evolution of the root means square deviation (r.m.s.d) of the trajectories

https://doi.org/10.1038/s41557-024-01620-y

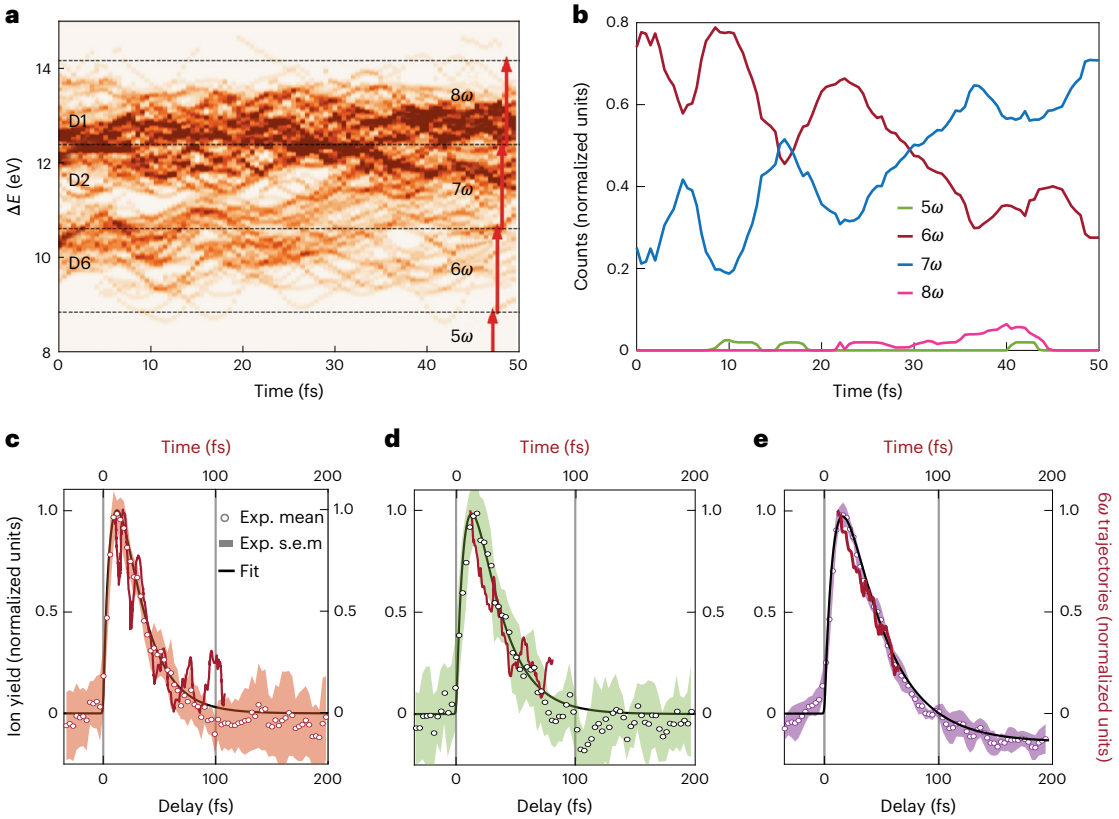

Fig. 4 | Sub-30-fs relaxation dynamics. a, Temporal evolution of the energy difference between the D1, D2 and D6 states of the cation and ground state of the dication for all the *p*-NA trajectories. The dotted horizontal black lines mark energy gaps for absorption of a VIS-NIR photon (represented by a red arrow). **b**, Normalized number of trajectories requiring five, six, seven and eight VIS-NIR photons (ω) to reach the ground state S0 of the dication in *p*-NA, for the trajectories initiated in the highest electronic states (D6). **c**–**e**, Normalized number of trajectories requiring the absorption of six VIS-NIR photons to reach S0 (dark red line) compared with the measured yields (circles and shaded area) for p-NA (**c**), m-NA (**d**) and nd-NA (**e**), obtained by integrating the TOF spectra of the high-energy NO^+ ion emitted in the forward direction (same as in Fig. 2d). To guide the eye, the fits to the experimental spectra are also indicated by thin continuous lines. Data are presented as mean values ± s.e.m.

with respect to the planar geometry, which corresponds to a local energy minimum. The r.m.s.d. serves as an indicator of the proximity of molecular structures to the planar minimum: the lower its value, the closer the system is to that minimum. As observed, the nuclear wave packet evolves toward a planar molecular geometry in ~7 fs after photoionization. A representative example of the nuclear dynamics associated with one of the trajectories is shown in Supplementary Video 4.

Sub-10-fs dynamics

We then computed the temporal evolution of the electron density in different regions of the moving molecular cation. The boundaries of the different regions, which change with time due to nuclear motion are defined by the basins of the electron density as defined in the electronic localization function (ELF) theory, as described in Methods.

The variation of the electron density in the vicinity of the NH_2 group is shown in Fig. 3b and, in more detail, in Supplementary Videos 1–3. During the first ~10 fs, the largest variations in the electron density occur around the NH_2 group and the adjacent C–N bond. Therefore, there is a substantial amount of ET from the lone pair of NH_2 toward the C–N bond (colour change from orange to green around the NH_2 group), which becomes a double bond (around 0.1 Å shorter; Extended Data Fig. 2). This is accompanied by planarization of the NH_2 group. During the following 10 fs, this group adopts a pyramidal structure again, albeit in the opposite direction, and the ET is reversed. To quantify the magnitude of the ET, Fig. 3c shows the evolution of the net charges that result from integration of the electron density over the two regions. ET amounts to almost a complete atomic unit of charge and goes in phase with planarization of the NH_2 group. In parallel, a significant ET from the NO_2 group to the corresponding adjacent C–N bond is observed (Extended Data Fig. 3 and Supplementary Videos 1–3). This ET, which is practically concerted with ET from the NH_2 group to the corresponding C–N bond and vice versa (except for a very small delay of 1–2 fs), also leads to the formation of a C=N double bond in this side of the molecule. Therefore, the signature of NH_2 planarization is also imprinted in the NO_2 group. The same ultrafast behaviour was obtained for *m*-NA and nd-NA, hence corroborating our theoretical interpretation. We note that this ET initiated by prompt ionization occurs in the same time interval as the initial increase of the yield for production of NO^+ and NO_2^+ fragments.

The temporal evolution of the nuclear kinetic energy and of the cation–dication Dyson norms shown in Fig. 3d allows us to confirm that the rise of the NO^+ and NO_2^+ yields at early times is indeed the signature of concerted NH_2 planarization and ET. As observed, the nuclear kinetic energy increases dramatically within the initial ~10 fs. This increase favours CE following the probe step, consequently promoting the production of NO^+ and NO_2^+ fragments. This is the consequence of the nuclear wave packet acceleration in the potential energy surface of the initial state while travelling towards the energy minimum associated with the planar structure. At longer times, the nuclear wave packet splits as the system goes through a series of conical intersections (Extended Data Fig. 4), leading to a more complex evolution. As a result, the average nuclear kinetic energy does not significantly increase further and fluctuates around a mean value. On its way to the minimum of the potential energy surface during the first 10 fs, the nuclear wave packet becomes progressively narrower, thus favouring

ionization by the probe pulse. This goes in parallel with a significant increase of the cation–dication Dyson norm in the same time interval (Fig. 3d and Supplementary Fig. 14g–i), which also favours ionization by the probe pulse.

Thus, it is the combined effect of increasing nuclear wave packet localization and nuclear kinetic energy that favours ionization of the cation by the probe pulse and the ensuing CE, which leads to a more efficient production of NO^+ and NO_2^+ fragments. Another fact that supports this interpretation is that the production yield of several charged fragments associated to the C–N bond, towards which the initial CT occurs, shows an ultrafast increase with a time constant of ~10 fs, implying that localization and higher kinetic energy also causes an increment in the probability of cation excitation over certain fragmentation barriers. These fragments (CN^+, C_2N^+ and C_3N^+) are connected to the promotion from the lowest excited states toward higher-lying cationic excited states, and show an exponential decay with a much longer time constant ($\tau_2 > 60$ fs; Supplementary Table 1) than that measured for the fragments resulting from dication generation and CE. Thus, we can now conclude that the time required for CT from the donor group to the ring, following the textbook scheme shown in Fig. 3e, is only ~10 fs. Moreover, in agreement with the commonly accepted picture, this CT requires that the nitrogen atom changes its hybridization from sp^3 (pyramidal) to sp^2 (planar) in only 10 fs. Due to these results, we can associate a timing of ~10 fs with this fundamental process of donor–acceptor systems. It is also important to emphasize here that the simulation times considered in the preceding analysis are too short to enable the observation of CT to further positions in the phenyl ring or the NO_2 acceptor group. Indeed, at variance with NH_2, the geometric changes needed to modify the electronic configurations in NO_2 take much longer due to the much larger mass of the oxygen atoms (as described in Supplementary Section 10). Thus, the charge transferred to the C–N bond can only go back and forth between this bond and NH_2 in the short time interval considered in the calculations. This back-and-forth motion of the charge is not observed in the experiment due to the sub-30-fs damping of the fragments resulting from CE.

Sub-30-fs dynamics

To understand the origin of this damping, Fig. 4a shows, for all calculated nuclear trajectories, the temporal evolution of the energy difference between the excited cationic states, populated by the attosecond pump pulses, and the ground state of the molecular dication, reached after the interaction with the VIS-NIR probe pulses. One can see that, whereas the energy required to reach the molecular dication from trajectories starting in the lowest states, D1 and D2, barely changes with time, there are trajectories starting in higher excited states for which the energy difference with the ground state of the dication increases progressively with time, especially after ~25 fs. This concerns the higher excited states of the cation with the largest Dyson norms: state D6 in *p*-NA, state D8 in *m*-NA and state D5 in nd-NA (Supplementary Table 3). Consequently, the number of VIS-NIR photons required to ionize the molecular cation increases with time, as illustrated in Fig. 4a, where the energies needed to ionize the molecular cation by absorption on *n* VIS-NIR photons at any time are shown. From this figure, we can estimate the number of trajectories which require absorption of a particular number of VIS-NIR photons to reach the dication. Figure 4b shows the normalized number of trajectories requiring five, six, seven and eight VIS-NIR photons to reach the ground state S0 of the dication (Fig. 1c) for the trajectories initiated in the cationic state D6 of *p*-NA. As displayed in Fig. 4c–e, the temporal evolution of the number of trajectories that require the absorption of six VIS-NIR photons to reach S0 closely follows the relaxation dynamics of the NO^+ yield of the three molecules. The decrease in the number of trajectories leads to an overall decrease in the probability of double ionization by a combination of the pump and probe pulses, hence hindering the production of the observed dication-related fragments. Our interpretation is consistent with both *m*-NA and nd-NA experimental and numerical results.

The experimental measurements do not reflect the charge oscillations in the slowly decreasing yield beyond 10 fs. This can probably be attributed to the stabilization and nearly random variation of the cation–dication Dyson norms and the average nuclear kinetic energy around a central value. This is in contrast to the rapid and monotonic increase of these quantities from 0 to 10 fs, as illustrated in Fig. 3d. Consequently, any traces of the clear oscillations of the charge, which persist up to significantly longer durations, should effectively be diminished. Unambiguous proof of this claim would necessitate modelling the ionization by the IR probe pulse and the subsequent coupled electron and nuclear dynamics up to sufficiently long times—ideally, comparable to the times needed by the ionic fragments to reach the detector. However, this is unfeasible for molecules of this complexity with currently available theoretical tools.

Interestingly, the ultrafast CT process remains unaffected by both the inductive effect and methylation. In the case of methylation, this can be attributed to the methyl groups being positioned closer to the planar geometry, thereby counterbalancing the impact of the increased mass of the donor group. At the same time, it is worth noting that the observed decay time for nd-NA ($\tau_2 = 31.4 \pm 1.3$ fs) is longer than in *p*-NA, suggesting a direct impact of methylation on nuclear wave packet confinement.

Conclusion

We have shown that the very first step of ET in prototypical nitroaniline cations, that is, CT from the NH_2 lone pair to the adjacent C–N bond, occurs in about 10 fs and is driven by planarization of the NH_2 group. This is the time needed by the nitrogen atom to change its hybridization from sp^3 to sp^2, so that an electron can effectively be transferred to the rest of the molecule. The electron dynamics observed in this study exhibit a slower rate compared to those documented in previous experimental[32,33] and theoretical[32,33,44–48] investigations of molecules incorporating donor and acceptor groups. In those studies, the observed electron dynamics arise from a coherent superposition of electronic states (that is, an electronic wave packet) in the molecular cation, induced by either a broadband attosecond pulse[32,33,44,47,48] or by the electron rearrangement that follows the sudden creation of a single 1h state in the molecule[45,46]. As the energy differences between the electronic states involved in these coherent superpositions are of the order of eletron-volts, the corresponding beatings must necessarily occur in the sub- or few-femtosecond timescale. This is not what we observe in the present work. The observed dynamics result from the coupled electron–nuclear motion triggered by the attosecond pulse in the molecular cation, where electronic charges redistribute following nuclear rearrangements. The dynamics are therefore necessarily slower than those reported in previous works. Nonetheless, they lead to changes of about 1 atomic unit of charge around the NH_2 group in just 10 fs, which still requires extreme time resolution to be resolved unambiguously. This process is at the heart of any subsequent ET/CT process occurring at longer timescales, where eventually the CT is completed toward the acceptor nitro group. We have also provided a comprehensive explanation for the decay of the ionic fragments that is observed in this and earlier XUV pump/VIS-NIR probe experiments at long pump–probe delays, which we believe to be a consequence of the increasing inefficiency of the probing step due to the continuous spreading of the nuclear wave packet.

The results reported here answer a fundamental question in chemistry as they unveil the times required to transfer charge from an electron donor unit to the adjacent carbon atom of the benzene ring, and for the concomitant required structural changes to occur. Therefore, we believe that these experimental and theoretical findings pave the way to a better understanding of the textbook diagrams and concepts used to qualitatively predict charge migration in organic molecules.

Online content

Any methods, additional references, Nature Portfolio reporting summaries, source data, extended data, supplementary information, acknowledgements, peer review information; details of author contributions and competing interests; and statements of data and code availability are available at https://doi.org/10.1038/s41557-024-01620-y.

References

1. Borrego-Varillas, R., Lucchini, M. & Nisoli, M. Attosecond spectroscopy for the investigation of ultrafast dynamics in atomic, molecular and solid-state physics. *Rep. Prog. Phys.* **85**, 066401 (2022).
2. Nisoli, M., Decleva, P., Calegari, F., Palacios, A. & Martín, F. Attosecond electron dynamics in molecules. *Chem. Rev.* **117**, 10760–10825 (2017).
3. Wörner, H. J. et al. Charge migration and charge transfer in molecular systems. *Struct. Dyn.* **4**, 061508 (2017).
4. Barber, J. Photosynthetic energy conversion: natural and artificial. *Chem. Soc. Rev.* **38**, 185–196 (2009).
5. Zhou, X. et al. Probing and controlling non-Born–Oppenheimer dynamics in highly excited molecular ions. *Nat. Phys.* **8**, 232–237 (2012).
6. Katayama, T. et al. Tracking multiple components of a nuclear wavepacket in photoexcited Cu(I)–phenanthroline complex using ultrafast X-ray spectroscopy. *Nat. Commun.* **10**, 3606 (2019).
7. Vacher, M., Mendive-Tapia, D., Bearpark, M. J. & Robb, M. A. Electron dynamics upon ionization: control of the timescale through chemical substitution and effect of nuclear motion. *J.Chem. Phys.* **142**, 094105 (2015).
8. Skourtis, S. S., Balabin, I. A., Kawatsu, T. & Beratan, D. N. Protein dynamics and electron transfer: electronic decoherence and non-Condon effects. *Proc. Natl Acad. Sci. USA* **102**, 3552–3557 (2005).
9. Arnold, C., Vendrell, O., Welsch, R. & Santra, R. Control of nuclear dynamics through conical intersections and electronic coherences. *Phys. Rev. Lett.* **120**, 123001 (2018).
10. Li, W. et al. A high-efficiency organic solar cell enabled by the strong intramolecular electron push–pull effect of the nonfullerene acceptor. *Adv. Mater.* **30**, 1707170 (2018).
11. Aradhya, S. V. & Venkataraman, L. Single-molecule junctions beyond electronic transport. *Nat. Nanotechnol.* **8**, 399–410 (2013).
12. Berrah, N. et al. Femtosecond-resolved observation of the fragmentation of buckminsterfullerene following X-ray multiphoton ionization. *Nat. Phys.* **15**, 1279–1283 (2019).
13. Castrovilli, M. C. et al. Ultrafast hydrogen migration in photoionized glycine. *J. Phys. Chem. Lett.* **9**, 6012–6016 (2018).
14. Wörner, H. J. et al. Conical intersection dynamics in NO_2 probed by homodyne high-harmonic spectroscopy. *Science* **334**, 208–212 (2011).
15. Picón, A. et al. Hetero-site-specific X-ray pump-probe spectroscopy for femtosecond intramolecular dynamics. *Nat. Commun.* **7**, 11652 (2016).
16. Al-Haddad, A. et al. Observation of site-selective chemical bond changes via ultrafast chemical shifts. *Nat. Commun.* **13**, 7170 (2022).
17. Lépine, F., Ivanov, M. Y. & Vrakking, M. J. J. Attosecond molecular dynamics: fact or fiction? *Nat. Photonics* **8**, 195–204 (2014).
18. Lutman, A. A. et al. Fresh-slice multicolour X-ray free-electron lasers. *Nat. Photonics* **10**, 745–750 (2016).
19. Duris, J. et al. Tunable isolated attosecond X-ray pulses with gigawatt peak power from a free-electron laser. *Nat. Photonics* **14**, 30 (2020).
20. Barillot, T. et al. Correlation-driven transient hole dynamics resolved in space and time in the isopropanol molecule. *Phys. Rev. X* **11**, 031048 (2021).
21. Kraus, P. M., Zürch, M., Cushing, S. K., Neumark, D. M. & Leone, S. R. The ultrafast X-ray spectroscopic revolution in chemical dynamics. *Nat. Rev. Chem.* **2**, 82–94 (2018).
22. Kobayashi, Y., Chang, K. F., Zeng, T., Neumark, N. M. & Leone, S. R. Direct mapping of curve-crossing dynamics in IBr by attosecond transient absorption spectroscopy. *Science* **365**, 79–83 (2019).
23. Timmers, H. et al. Disentangling conical intersection and coherent molecular dynamics in methyl bromide with attosecond transient absorption spectroscopy. *Nat. Commun.* **10**, 3133 (2019).
24. Zinchenko, K. S. et al. Sub-7-femtosecond conical-intersection dynamics probed at the carbon K-edge. *Science* **371**, 489–494 (2021).
25. Ridente, E. et al. Femtosecond symmetry breaking and coherent relaxation of methane cations via X-ray spectroscopy. *Science* **380**, 713–717 (2023).
26. Matselyukh, D. T., Despré, V., Golubev, N. V., Kuleff, A. I. & Wörner, H. J. Decoherence and revival in attosecond charge migration driven by non-adiabatic dynamics. *Nat. Phys.* **18**, 1206–1213 (2022).
27. Galli, M. et al. Generation of deep ultraviolet sub-2-fs pulses. *Opt. Lett.* **44**, 1308–1311 (2019).
28. Reduzzi, M. et al. Direct temporal characterization of sub-3-fs deep UV pulses generated by resonant dispersive wave emission. *Opt. Express* **31**, 26854–26864 (2023).
29. Attar, A. R. et al. Femtosecond X-ray spectroscopy of an electrocyclic ring-opening reaction. *Science* **356**, 54–59 (2017).
30. Chang, K. F. et al. Revealing electronic state-switching at conical intersections in alkyl iodides by ultrafast XUV transient absorption spectroscopy. *Nat. Commun.* **11**, 4042 (2020).
31. Chang, K. F. et al. Mapping wave packet bifurcation at a conical intersection in CH3I by attosecond XUV transient absorption spectroscopy. *J. Chem. Phys.* **154**, 234301 (2021).
32. Calegari, F. et al. Ultrafast electron dynamics in phenylalanine initiated by attosecond pulses. *Science* **346**, 336–339 (2014).
33. Lara-Astiaso, M. et al. Attosecond pump–probe spectroscopy of charge dynamics in tryptophan. *J. Phys. Chem. Lett.* **9**, 4570–4577 (2018).
34. Ludwig, A. et al. Ultrafast relaxation dynamics of the ethylene cation $C_2H_4^+$. *J. Phys. Chem. Lett.* **7**, 1901–1906 (2016).
35. Lucchini, M. et al. Few-femtosecond $C_2H_4^+$ internal relaxation dynamics accessed by selective excitation. *J. Phys. Chem. Lett.* **13**, 11169–11175 (2022).
36. Hervé, M. et al. Ultrafast dynamics of correlation bands following XUV molecular photoionization. *Nat. Phys.* **17**, 327–331 (2020).
37. Carey, F., Giuliano, R., Allison, N., & Bane, S. *Organic Chemistry* 11th edn (McGraw-Hill, 2019).
38. Aviram, A. & Ratner, M. Molecular rectifiers. *Chem. Phys. Lett.* **29**, 277–283 (1974).
39. Xin, N. et al. Concepts in the design and engineering of single-molecule electronic devices. *Nat. Rev. Phys.* **1**, 211–230 (2019).
40. Leary, E. et al. Incorporating single molecules into electrical circuits. The role of the chemical anchoring group. *Chem. Soc. Rev.* **44**, 920–942 (2015).
41. Montgomery, J. A. Jr., Frisch, M. J., Ochterski, J. W. & Petersson, G. A. A complete basis set model chemistry. VII. Use of the minimum population localization method. *J. Chem. Phys.* **112**, 6532–6542 (2000).
42. Olsen, J. The CASSCF method: a perspective and commentary. *Int. J. Quantum Chem.* **111**, 3267–3272 (2011).
43. Richter, M., Marquetand, P., González-Vázquez, J., Sola, I. & González, L. SHARC: ab initio molecular dynamics with surface hopping in the adiabatic representation including arbitrary couplings. *J. Chem. Theory Comput.* **7**, 1253–1258 (2011).
44. Vacher, M., Bearpark, M. J., Robb, M. A. & Malhado, J. P. Electron dynamics upon ionization of polyatomic molecules: coupling to quantum nuclear motion and decoherence. *Phys. Rev. Lett.* **118**, 083001 (2017).

45. Kuleff, A. I., Lünnemann, S. & Cederbaum, L. S. Ultrafast charge migration following valence ionization of 4-methylphenol: jumping over the aromatic ring. *J. Phys. Chem A* **114**, 8676–8679 (2010).
46. Folorunso, A. S. et al. Attochemistry regulation of charge migration. *J. Phys. Chem. A* **127**, 1894–1900 (2023).
47. Lara-Astiaso, M. et al. Decoherence, control and attosecond probing of XUV-induced charge migration in biomolecules. A theoretical outlook. *Faraday Disc.* **194**, 41–59 (2016).
48. Ayuso, D., Palacios, A., Decleva, P. & Martín, F. Ultrafast charge dynamics in glycine induced by attosecond pulses. *Phys. Chem. Chem. Phys.* **19**, 19767–19776 (2017).

Methods

Molecular target

The three samples under investigation (*p*-NA (CAS number 100-01-6), *m*-NA (CAS number 99-09-2) and nd-NA (CAS number 100-23-2)) were acquired from Sigma-Aldrich. The samples, which are in the form of a powder at standard ambient temperature and pressure, are stable at room temperature and were used without further purification. An effusive oven source was used to evaporate the samples in a vacuum environment. The powder was loaded into a hollowed screw, which was subsequently inserted into the oven. A heating cable was used to increase the temperature. The temperature required for the sublimation of the samples was in the range between 90 °C and 110 °C, well below their melting points. Argon was used as a carrier gas to transport the molecules to the interaction region, while simultaneously reducing their internal kinetic energy before the interaction.

Photoelectron–photoion coincidence experiments with synchrotron radiation

Photoemission experiments were performed at the Gas Phase Photoemission (GAPH) beamline[49] of the Elettra synchrotron radiation facility (Trieste, Italy) at photon energies of 60 eV and 37 eV. The former energy is suitable for obtaining a complete picture of the valence electron states, whereas the latter mimics the central frequency of the attosecond pulses used in the pump–probe measurements. Molecular samples were sublimated using an oven source. The experimental station hosts a VG 220i hemispherical electron analyser equipped with a 2D position-sensitive detector and a Wiley–McLaren TOF mass spectrometer, mounted opposite to each other at the magic angle (~55°) with respect to the polarization axis of the radiation[50]. The electron and ion spectrometers have been used either independently of each other for PES and photoion mass spectrometry or in combination for photoelectron–photoion coincidence (PEPICO) experiments. In the PES experiments the analyser was operated with a pass energy of 10 eV, which results in an energy resolution of ~200 meV, and the photoelectron yield is measured versus the kinetic energy, which is directly related to the binding energy, BE (BE = photon energy − photoelectron energy) of the different ionic states.

The PEPICO spectra were acquired at a fixed photon energy of 60 eV with an analyser pass energy of 30 eV and scanning the electron kinetic energy over the binding energy region 8–32 eV in steps of 2.7 eV to obtain a sufficient overlap between adjacent acquisition windows. The experimental chamber was maintained at a background pressure $\leq 1 \times 10^{-7}$ mbar. In a PEPICO experiment, both photoelectrons and photoions from the same photoionization event are detected in coincidence. Although this method introduces complexities in the experimental configuration, data acquisition and data management, it provides a direct view of the various decay channels and their dependence on BE. The 3D plot of Extended Data Fig. 1 displays the yield of electron–ion coincidences for selected m/q ion as a function of BE. Integration along the m/q axis yields the photoelectron spectrum (orange line in Extended Data Fig. 1), while integration across the BE axis gives the ion mass spectrum (pink line in Extended Data Fig. 1).

Extended Data Fig. 5 shows a zoom of the PEPICO data around $m/q = 30$ (corresponding to NO^+) for the three investigated molecules. A notable broadening of the mass spectra was measured for BEs above ~22 eV, which corresponds to the calculated threshold for dication formation (Fig. 1c): this is the signature of the dissociation of an unstable dication following CE. For BEs in the range 15–22 eV, the mass spectra are characterized by a sharp peak, the relative amplitude of which with respect to the broadened structure at higher BEs depends on the particular molecules. This peak is pronounced in the case of *p*-NA and is less prominent in the case of *m*-NA and nd-NA. This is in agreement with the mass spectra measured with our attosecond beamline, after XUV excitation, as shown in Extended Data Fig. 6.

A similar behaviour was measured for the cation NO_2^+ ($m/q = 46$), thus supporting the conclusion that the formation of this fragment is also driven by CE) of an unstable dication. This is consistent with the observation that the measured temporal evolution of the NO_2^+ yield is very similar to that of the NO^+ cation (as shown in Supplementary Fig. 5).

Photoelectron–photoion photoion coincidence experiments with synchrotron radiation

We have also performed photoelectron–photoion photoion coincidence (PEPIPICO) measurements at the Elettra synchrotron radiation facility. The fundamental concept underlying the PEPIPICO technique involves detecting two positive ions generated from a single CE process following photon absorption. The starting time for triggering the measurement of the ion arrival times is provided by the detection of a photoelectron. Through PEPIPICO measurements, valuable information is obtained regarding the formation of ion pairs stemming from the same ionization event. Extended Data Fig. 7a depicts a close-up view of the ion–ion coincidence map within the TOF range in which correlations between ion pairs with $m/q = 30$ and $m/q = 108$ $(M–NO)^+$ are expected. Extended Data Fig. 7b illustrates the TOF region of interest pertaining to the ionic pair $m/q = 46$ and $m/q = 92$. The blue dots represent coincidence events corresponding to photoelectron BEs exceeding 20 eV (dication formation threshold), and red dots denote BEs below 20 eV. For BEs exceeding 20 eV the calculated Pearson linear correlation coefficient, ranging from 0.3 to 0.6, reveals a correlation between the formation of the fragments with $m/q = 30$ and $m/q = 108$ and similarly for the ionic pair $m/q = 46$ and $m/q = 92$. However, a negligible correlation, indicated by a Pearson linear correlation coefficient <0.05, is observed for BEs below the dication formation threshold. Additionally, it is noticeable that the region of correlation (represented by the blue dots) aligns with a diagonal of slope −1, suggesting that the detected co-ions adhere to momentum conservation. Statistical valuation of the slope reveals linear coefficients of −1.16 and −0.89 for the 30–108 and 46–92 pairs, respectively.

Therefore, from the PEPIPICO measurements it is possible to conclude that in the case of *p*-NA, the appearance of ions with $m/q = 30$ resulting from CE correlates with the production of the co-fragments with $m/q = 108$. Likewise, the co-fragment corresponding to ions with $m/q = 46$ was determined to be $m/q = 92$. This trend is observed for the three investigated molecular species.

Nuclear dynamics calculations

Semiclassical surface-hopping (SH) trajectories using Tully's fewest-switches algorithm, as implemented in the SHARC[43] code, were calculated to simulate the coupled electron–nuclear dynamics triggered after the initial XUV photoionization. In this implementation the nuclei are propagated using Newton's equations with the velocity Verlet algorithm. The temporal evolution of the coefficients of the configuration interaction vector describing the electronic wavefunction is given by the following equation

$$\frac{\partial c_\beta}{\partial t} = -\sum_\alpha \left\{ \frac{i}{\hbar} H_{\beta\alpha}[\mathbf{R}(t)] + K_{\beta\alpha}[\mathbf{R}(t)] \right\} c_\alpha \quad (1)$$

where c_β is the CI coefficient of the β electronic state, $H_{\beta\alpha}[\mathbf{R}(t)] = \langle \psi_\beta[\mathbf{R}(t);\mathbf{r}'] | H_{\text{eff}}[\mathbf{R}(t);\mathbf{r}'] | \psi_\alpha[\mathbf{R}(t);\mathbf{r}'] \rangle$ represents the diabatic Hamiltonian whose diagonal elements are the different potentials and the off-diagonal elements are the Hamiltonian couplings between the diabatic states, and $K_{\beta\alpha} = \langle \psi'_\alpha[\mathbf{R}(t)], |, \frac{\partial}{\partial t}, |, \psi_\beta[\mathbf{R}(t+\Delta t)] \rangle$ with $\psi'_\alpha[\mathbf{R}(t)]$ being the diabatic state α obtained from the maximization of the adiabatic overlap computed with OpenMOLCAS (v. 18.09) using the bi-orthonormalization algorithm. Although equation (1) is solved in the diabatic picture, the SH probability is calculated in the adiabatic representation using the density flux formalism proposed by Petersen and Mitrić[51].

For each molecule, the initial conditions (geometries and velocities) of the nuclei in each of the propagated trajectories were obtained

using a Wigner distribution centred around the equilibrium geometry. This is necessary to mimic the initial zero-point-energy geometry distribution of the neutral molecule. To achieve full convergence in molecules of this size, one should ideally use a few thousand geometries in the Wigner distribution for each initial state. However, this is computationally very demanding, and therefore we have followed common practice and checked that 100 geometries provide a reasonable description of the initial state. The corresponding trajectories were then propagated for a total of 50 fs with a time step of 0.5 fs and using 51 substeps for the solution of equation (1) for all states highlighted in blue in Supplementary Table 3.

Results of the SH simulations: state populations, bond lengths and charge dynamics

As an illustration, Extended Data Fig. 4 shows the evolution of the population of all adiabatic states included in the SH calculations for *p*-NA (dynamics started in the D6 state, that is, the representative example discussed in the main text). As can be seen, during the first 5–7 fs, the population of the initial D6 state rapidly decreases and that of the D4, D5 and D7 states increases. At around 7 fs, the population in the latter states becomes comparable to that in the D6 state.

This is due to non-adiabatic transitions occurring in the vicinity of a series of conical intersections between these states. As we will show below, during the first few tens of femtoseconds, the dynamics resulting from SH simulations starting from different initial states are very similar. Therefore, the observed abrupt changes in the relative population of the states do not lead to similarly abrupt changes in the charge dynamics. At much longer times, however, this may not be the case, but with the present experiment it is not possible to get information for these longer times.

For the same case as above, Extended Data Fig. 2 shows the evolution of the two C–N and the six C–C bond lengths with time. As it can be seen, NH_2 planarization during the first 10 fs is accompanied by a reduction of about 0.1 Å in the two C–N bond lengths. At longer times, as NH_2 goes back to its initial pyramidal geometry, the C–N bond lengths also go back to their initial values. This cycle repeats basically with the same frequency as the planarization–pyramidalization motion. For the C–C bond lengths, similarly simple regular patterns are not observed. We note that the NO_2 group remains planar throughout the entire interval considered in Extended Data Fig. 2 (50 fs). As shown in Supplementary Section 10, deplanarization of this group occurs at much longer times.

Extended Data Fig. 3 shows snapshots of the evolution of the electronic density in the NO_2 region and the evolution of the average charge in the ELF basins for the N–O bonds group and the C–N bond connecting it to the ring. A significant amount of charge transfer from the NO_2 group to the adjacent C–N bond is observed (see also Supplementary Videos 1–3). This transfer of charge, which is practically concerted with that from NH_2 to the corresponding C–N bond (Fig. 3), except for a very small delay of 1–2 fs, leads to the formation of the C=N double bond described above.

Data availability

The experimental data and the results of the simulations discussed in this work are available via Zenodo at https://doi.org/10.5281/zenodo.12759592 (ref. 52).

Code availability

SHARC implementation is available via Zenodo at https://doi.org/10.5281/zenodo.7352971 (ref. 53). OpenMOLCAS (v. 18.09) is available at https://gitlab.com/Molcas/OpenMolcas.git. Multiwfn (v. 3.8) is available at http://sobereva.com/multiwfn/. Tiresia (v. 1) is available via Mendeley Data at https://doi.org/10.17632/fcrjxwgjxh.

References

49. Blyth, R. R. et al. The high resolution gas phase photoemission beamline, Elettra. *J. Electron Spectrosc. Relat. Phenom.* **101–103**, 959–964 (1999).
50. Chiarinelli, J. et al. Electron and ion spectroscopy of the cyclo-alanine–alanine dipeptide. *Phys. Chem. Chem. Phys.* **24**, 5855–5867 (2022).
51. Petersen, J. & Mitrić, R. Electronic coherence within the semiclassical field-induced surface hopping method: strong field quantum control in K_2. *Phys. Chem. Chem. Phys.* **14**, 8299 (2012).
52. Nisoli, M., Martín, F., & Martín, N. Data from the manuscript: 'Few-femtosecond electron transfer dynamics in photoionized donor-pi-acceptor molecules'. *Zenodo* https://doi.org/10.5281/zenodo.12759592 (2024).
53. sharcdyn/sharc_public: Debug for MD-GAS 2023 Gdansk (Version v1). *Zenodo* https://doi.org/10.5281/zenodo.8120776 (2023).

Acknowledgements

We thank J. Cachón and P. Recio for their help in the first stages of this project. We thank J. Travers and C. Brahms for the development of the stretching technique and gas cell design used in the hollow capillary compressor set-up. This project has received funding from the European Research Council (ERC) under the European Union's Horizon 2020 research and innovation programme (grant agreement number 951224, TOMATTO, N.M., F.M. and M.N.), from MIUR PRIN number 20173B72NB (P.B., L.A. and M.N.), from the Spanish Ministry of Science and Innovation under grant PID2021-122839NB-I00 (L.B.) and from Laserlab-Europe EU-H2020 grant agreement number 654148, project CUSBO002616 (L.B.). It is based upon work from COST Action CA18222 (AttoChem), supported by COST (European Cooperation in Science and Technology).

Author contributions

M.N., F.M. and N.M. conceived the project. M.N., R.B.-V., M.R. and M.L. coordinated the time-resolved measurements. F.V., D.M., Y.W., F.H. and L. Colaizzi. performed the time-resolved measurements and contributed to the definition of the experimental procedures. R.B.-V., P.B., L.A. and R.R. coordinated the synchrotron measurements at Elettra, performed by L. Carlini., M.C.C., R.B.-V, F.V., R.R. and P.B. J.G.-V., A.P. and F.M. coordinated the theoretical calculations. F.F.-V., J.G.-V. and J.D. performed the theoretical calculations and contributed to the definition of the theoretical methods. All authors contributed to the discussion of the results. M.N., F.V., F.M. and F.F.-V. wrote the first version of the paper, to which all authors contributed.

Competing interests

The authors declare no competing interests.

Additional information

Extended data is available for this paper at https://doi.org/10.1038/s41557-024-01620-y.

Supplementary information The online version contains supplementary material available at https://doi.org/10.1038/s41557-024-01620-y.

Correspondence and requests for materials should be addressed to Rocío Borrego-Varillas, Fernando Martín or Mauro Nisoli.

Peer review information *Nature Chemistry* thanks the anonymous reviewers for their contribution to the peer review of this work.

https://doi.org/10.1038/s41557-024-01620-y

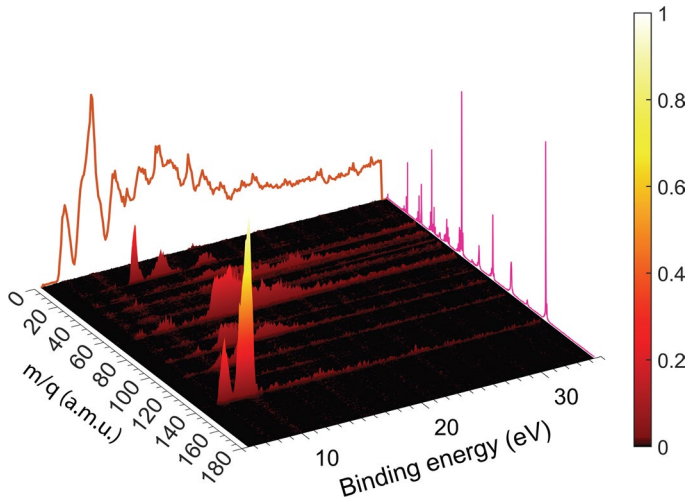

Extended Data Fig. 1 | PEPICO measurements. 3D plot of the PEPICO matrix for p-NA. The x-axis represents the binding energy (BE), the y-axis the mass to charge ratio (m/q) and the z-axis the number of events collected at the detector normalized to the maximum number of events. The solid orange line is the photoelectron spectrum while the pink solid line is the ion mass spectrum.

https://doi.org/10.1038/s41557-024-01620-y

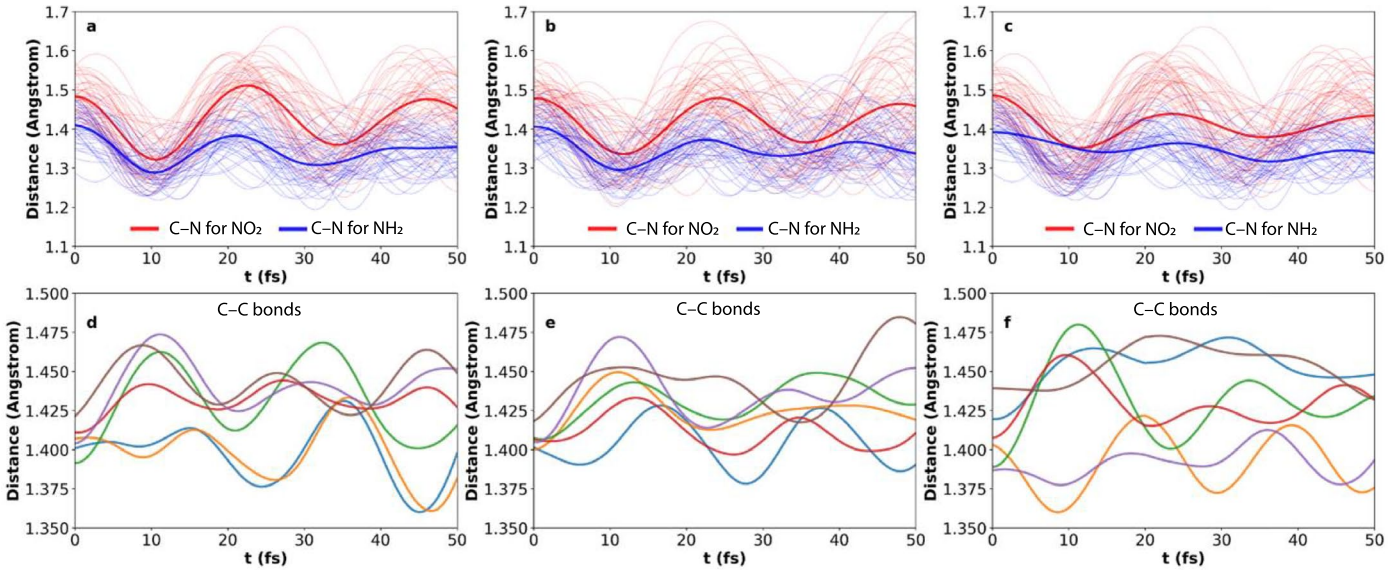

Extended Data Fig. 2 | C–N and C–C bond lengths for p-NA. Variation of the C–N (top panels) and C–C (lower panels) bond lengths for p-NA (panels **a, d**), m-NA (panels **b, e**) and nd-NA (panels **c, f**). The dynamics was started from the D6 state of p-NA, D8 state of m-NA and D5 state from nd-NA.

https://doi.org/10.1038/s41557-024-01620-y

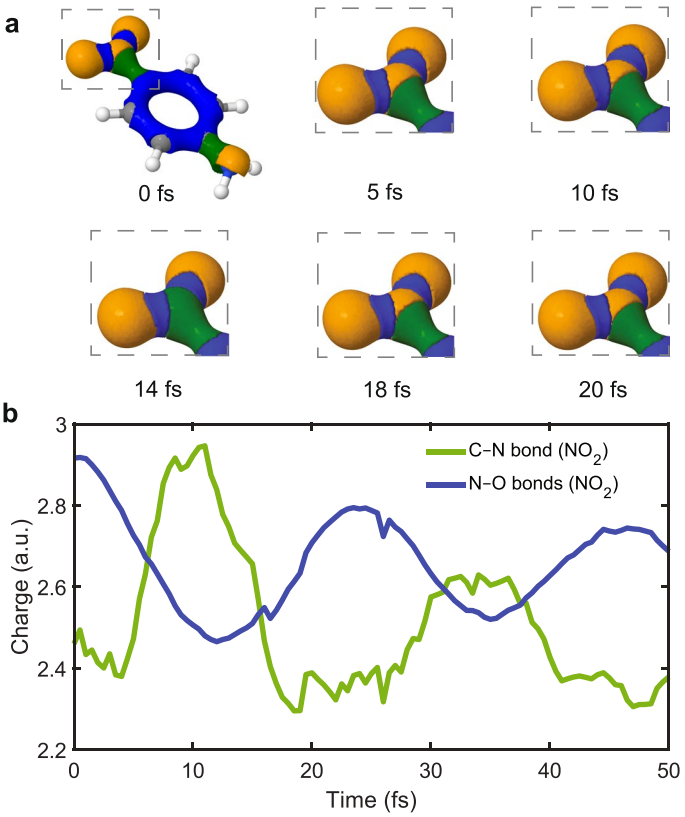

Extended Data Fig. 3 | Evolution of the electronic density in the NO_2 region. (**a**) Snapshots of the evolution of the electronic density. The colours indicate the basins where the density is assigned. In the NO_2 region, blue indicates the N–O bonds while green indicates C–N bond. (**b**) Temporal evolution of the average charge in the ELF basins for the N–O bonds group (blue) and the C–N bond connecting it to the ring (green).

https://doi.org/10.1038/s41557-024-01620-y

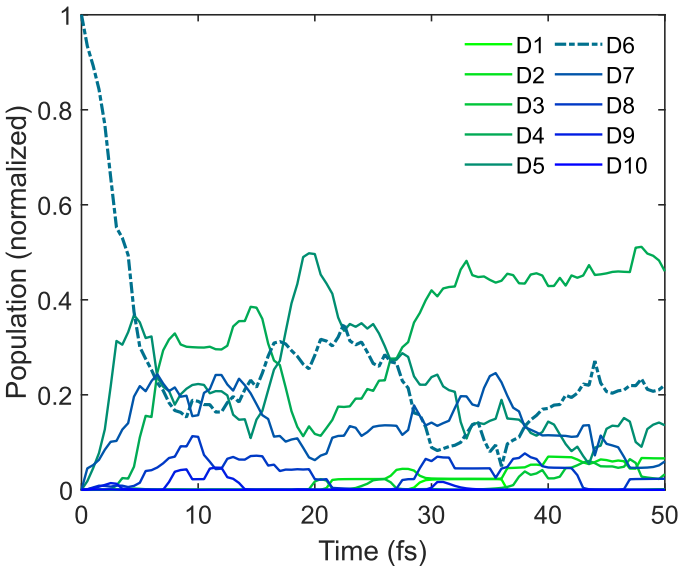

Extended Data Fig. 4 | Evolution of the population of adiabatic states of p-NA. Time evolution of the population of all adiabatic states included in the SH calculations initiated in the D6 state of p-NA.

https://doi.org/10.1038/s41557-024-01620-y

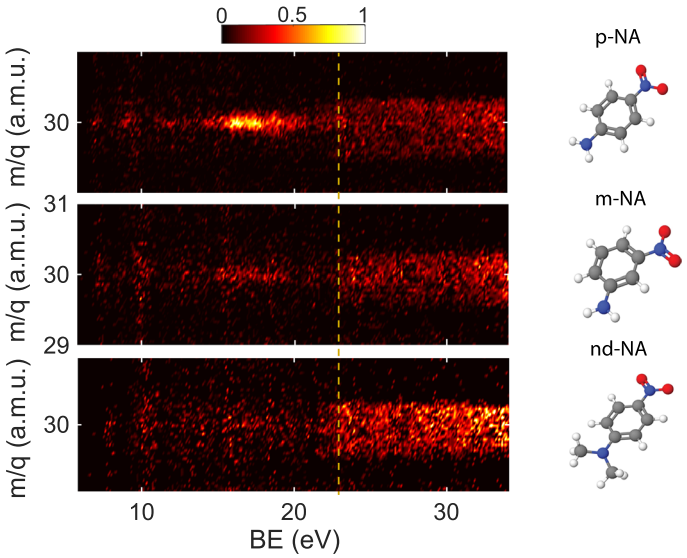

Extended Data Fig. 5 | Coulomb Explosion. Zoom of PEPICO measurements around $m/q = 30$ (NO^+) for the three investigated molecules, whose chemical structures are reported in the right column. The yellow dashed line shows the dication appearance energy.

https://doi.org/10.1038/s41557-024-01620-y

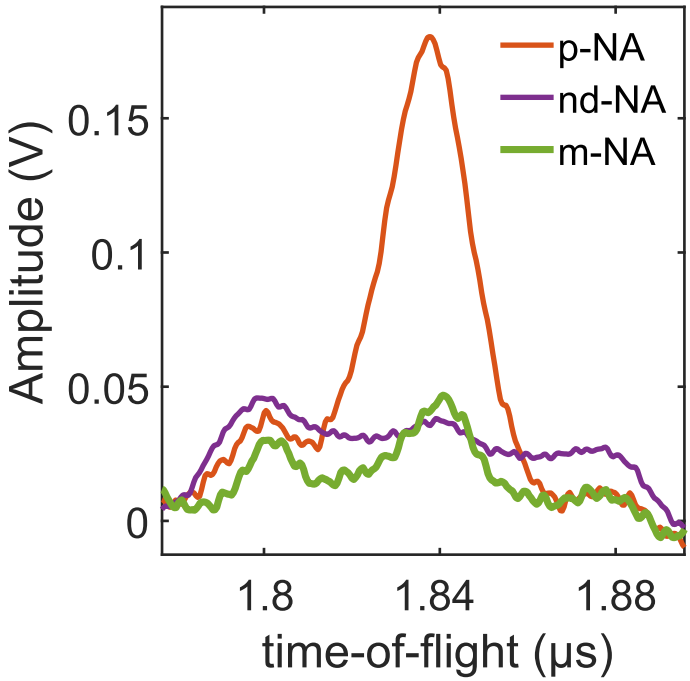

Extended Data Fig. 6 | Mass spectra produced by attosecond excitation. Mass spectra around fragment NO^+ ($m/q = 30$) of p-NA (orange), m-NA (green) and nd-NA (purple) measured by using the attosecond beamline after XUV excitation.

https://doi.org/10.1038/s41557-024-01620-y

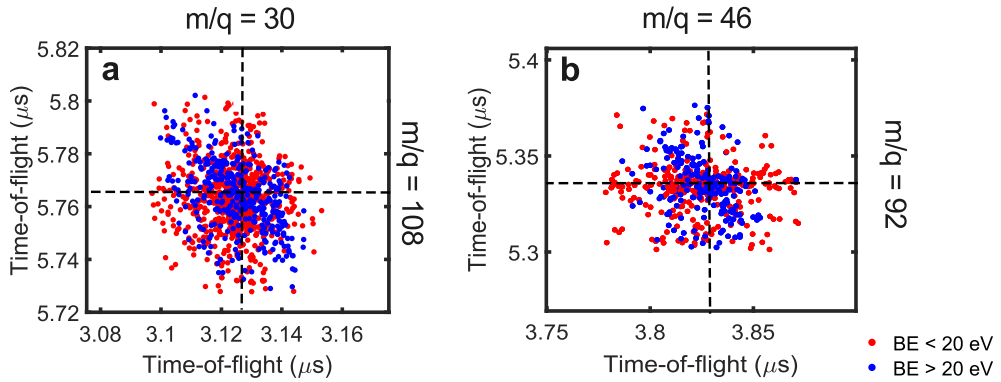

Extended Data Fig. 7 | PEPIPICO measurements in p-NA. Ion-ion coincidence map of p-NA within the time-of-flight range where correlations between ion pairs with $m/q = 30$ and $m/q = 108$ (**a**) and between ion pairs with $m/q = 46$ and $m/q = 92$ (**b**) are expected.